ELSEVIER

# The MUNU experiment, general description

## MUNU Collaboration

### (Bochum–Grenoble–Neuchâtel–Padova–Zürich)

C. Amsler[a], M. Avenier[b], G. Bagieu[b], C. Barnoux[b], H.-W. Becker[c], R. Brissot[b],
C. Broggini[d], J. Busto[e], J.-F. Cavaignac[b], J. Farine[e], D. Filippi[d], G. Gervasio[e],
P. Giarritta[a], G. Grgić[e], B. Guerre Chaley[b], V. Joergens[e,1] D.H. Koang[b], D. Lebrun[b],
R. Luescher[e], F. Mattioli[d], M. Negrello[d], F. Ould-Saada[a], A. Paić[e], O. Piovan[d],
G. Puglierin[d], D. Schenker[e], A. Stutz[b], A. Tadsen[e], M. Treichel[e,2],
J.-L. Vuilleumier[e,*], J.-M. Vuilleumier[e]

[a] *Physik -Institut, Winterthurerstrasse 190, CH-8057 Zürich, Switzerland*
[b] *Institut des Sciences Nucléaires, IN2P3-UJF, 53 avenue des Martyrs, F-38026 Grenoble Cedex, France*
[c] *Experimentalphysik III, Ruhr-Universität-Bochum, Universitätsstrasse 150, D-44780 Bochum, Germany*
[d] *Istituto Nazionale di Fisica Nucleare-Sezione di Padova and Università di Padova, via Marzolo 8, I-35131 Padova, Italy*
[e] *Institut de Physique, A.-L. Breguet 1, CH-2000 Neuchâtel, Switzerland*

## Abstract

We are building a low background detector based on a gas time projection chamber surrounded by an active anti-Compton shielding. The detector will be installed near a nuclear reactor in Bugey for the experimental study of $\bar{\nu}_e e^-$ scattering. We give here a general description of the experiment, and an estimate of the expected counting rate and background. The construction of the time projection chamber is described in details. Results of first test measurements concerning the attenuation length and the spatial as well as energy resolution in the $CF_4$ fill gas are reported.

## 1. Introduction

The MUNU experiment has been designed to study $\bar{\nu}_e e^-$ scattering with low-energy antineutrinos from a nuclear reactor. This process, as well as $\nu_e e^-$ scattering, is fundamental, and a precise investigation may provide information on basic features of the weak interaction, and on neutrino properties.

Both charged (CC) and neutral weak currents (NC) are involved. They are expected to interfere if the NC and CC final state neutrinos are identical, as assumed in the Standard Model [1]. A measurement of the differential cross section allows, in principle, to determine the Weinberg angle $\sin^2 \theta_W$ and to observe the interference which is expected to be destructive for reasonable values of $\sin^2 \theta_W$. Practically however $\bar{\nu}_e e^- \to \bar{\nu}_e e^-$ only has a good sensitivity to both effects, while $\nu_e e^- \to \nu_e e^-$ essentially probes the interference.

In addition, provided their magnetic moments are nonvanishing, neutrinos will have electromagnetic interactions, making them scatter from a left-handed active state, from the point of view of weak interaction, into a sterile right-handed state.

---

* Corresponding author. Tel.: +41 32 718 2906; fax: +41 32 718 2901; e-mail: jean-luc.vuilleumier@iph.unine.ch.

[1] Present address: Laboratori Nazionali del Gran Sasso, I-67010 Assergi, Italy.

[2] Present address: CERN, CH-1211 Genève 23, Switzerland.

The differential cross section for $\bar{\nu}_e e^-$ or $\nu_e e^-$ scattering is given by [1,2]

$$\frac{d\sigma}{dT} = \frac{G_F^2 m_e}{2\pi}\left[(g_V + x + g_A)^2 + (g_V + x - g_A)^2\left(1 - \frac{T}{E_\nu}\right)^2\right.$$

$$\left. + (g_A^2 - (g_V + x)^2)\frac{m_e T}{E_\nu^2}\right] + \frac{\pi\alpha^2\mu_\nu^2}{m_e^2}\frac{1 - T/E_\nu}{T} \qquad (1)$$

with $E_\nu$ the incident neutrino energy, and $T$ the electron recoil energy. Here the first line gives the contribution of the weak interaction to $\nu_e(\bar{\nu}_e)e^- \rightarrow \nu_e(\bar{\nu}_e)e^-$ scattering, with

$$g_V = 2\sin^2\theta_W + \frac{1}{2}, \qquad g_A = \begin{cases} \frac{1}{2} & \text{for } \nu_e, \\ -\frac{1}{2} & \text{for } \bar{\nu}_e \end{cases}$$

in the Standard Model; $x$ is calculated from the neutrino form factors, for Dirac neutrinos it is related to the square charge radius $\langle r^2 \rangle$ of the neutrino

$$x = \frac{2M_W^2}{3}\langle r^2 \rangle\sin^2\theta_W \quad \text{for } \nu_e, \ x \rightarrow -x \quad \text{for } \bar{\nu}_e. \qquad (2)$$

The second line in Eq. (1) gives the contribution from $\nu_e(\bar{\nu}_e)e^- \rightarrow \nu_\ell(\bar{\nu}_\ell)e^-$ ($\ell = e, \mu, \tau \dots$), with

$$\mu_\nu = \sqrt{\sum_\ell |\mu_{e\ell}|^2},$$

the effective magnetic moment, and $\mu_{\ell,\ell'}$ the neutrino magnetic moment matrix [3]. This matrix can either be Dirac like, in which case both static ($\ell = \ell'$) and transition ($\ell \neq \ell'$) moments may be non-zero, or Majorana like, in which case the transition moments only may be finite, the static moments being exactly zero.

## 1.1. The neutrino magnetic moment

The magnetic moment of the neutrino is an interesting feature. Models exist in which it can become relatively large, while the masses remain reasonably small [4–9]. If large enough, the magnetic moment will affect the cross section for all neutrino interactions, and cause neutrinos to precess in magnetic fields. This may lead to important effects in astrophysical systems.

Such a moment might be responsible for the observed low flux of $\nu_e$ from the sun in the $^{37}$Cl [10], GALLEX [11], SAGE [12], and Kamiokande [13] experiments. The most popular explanation is resonant neutrino oscillations in the matter of the sun (see Ref. [14]). But, as an alternative, one may invoke a neutrino magnetic moment of order $10^{-10}$–$10^{-12}\mu_B$, causing the neutrinos to flip from the left-handed original $\nu_e$ flavor eigenstate to a right-handed sterile state in the sun's magnetic field [3,15,16].

Other astrophysical observations suggest that moments of that order would be of the Majorana type. Indeed if neutri-

nos were Dirac particles, then the observed duration (several seconds) of the SN1987A neutrino burst implies much smaller values: $\mu_{\ell,\ell'} < 1$–$20 \times 10^{-13}\mu_B$ [17–19]. These limit assume that right-handed neutrinos are sterile and can escape from the supernova, and in any case do not apply to Majorana neutrinos. Limits from stellar cooling apply to both Dirac and Majorana neutrinos, but are less stringent: $\mu_{\ell,\ell'} < 10^{-12}$–$10^{-11}\mu_B$ [2,20–23]. This is not in strong conflict with magnetic moments of the strength considered, if one takes into account the model dependence of the astrophysical calculations.

Clearly, it is desirable to obtain unambiguous informations on the neutrino magnetic moment in laboratory experiments, in particular on that of the electron neutrino. The best way to do so is precisely to study in detail $\nu_e(\bar{\nu}_e)e^-$ scattering. The contribution of the weak interaction terms to the total cross-section increases linearly with $E_\nu$. The corresponding contribution from the magnetic moment interaction increases only logarithmically. Experiments with low energy neutrinos are thus best suited.

## 2. Present experimental situation

Beam dumps at intermediate energy accelerators produce $\nu_e$ with energies from 0 to 50 MeV. The fluxes are not very high however, and the $\nu_e$ are accompanied by equal numbers of $\nu_\mu$ and $\bar{\nu}_\mu$, which complicates the interpretation of the experimental data. A measurement of $\nu_e e^- \rightarrow \nu_e e^-$ scattering has been performed at the LAMPF beam dump [24]. In spite of a limited statistics the experiment showed that there was no room for a constructive interference, and confirmed the destructive interference. As expected the experiment did not give a precise value for the Weinberg angle. It produced however an upper limit for the magnetic moment of the $\nu_e$: $\mu_\nu < 1.08 \times 10^{-9}\mu_B$ [25].

Nuclear reactors produce lower-energy neutrinos, and are thus more attractive. They are copious sources of $\bar{\nu}_e$ with energies between 0 and 8 MeV and are ideally suited for such an experiment. The energy spectra are known with good precision, better than 3% for $E_\nu$ between 1.5 and 8 MeV [2,26,27]. Fig. 1 shows the expected electron recoil spectra at a $^{235}$U reactor, using Eq. (1) and taking $\sin^2\theta_W = 0.226$. The contribution of the weak interaction is shown, as well as that from a magnetic moment $\mu_\nu = 10^{-10}\mu_B$ alone. One sees that the lower the electron recoil the better the sensitivity to the magnetic moment.

Only few attempts have been made to measure $\bar{\nu}_e e^-$ scattering. The UC Irvine group led by Reines [28] built the first dedicated detector, which was operated successfully at the Savannah River Plant (SRP), observing the process for the first time. The detector consisted of a 15.9 kg plastic scintillator, coarsely segmented and surrounded by a NaI counter, a Pb shield and a liquid scintillator to veto cosmics. The signature for a good event was given by a single
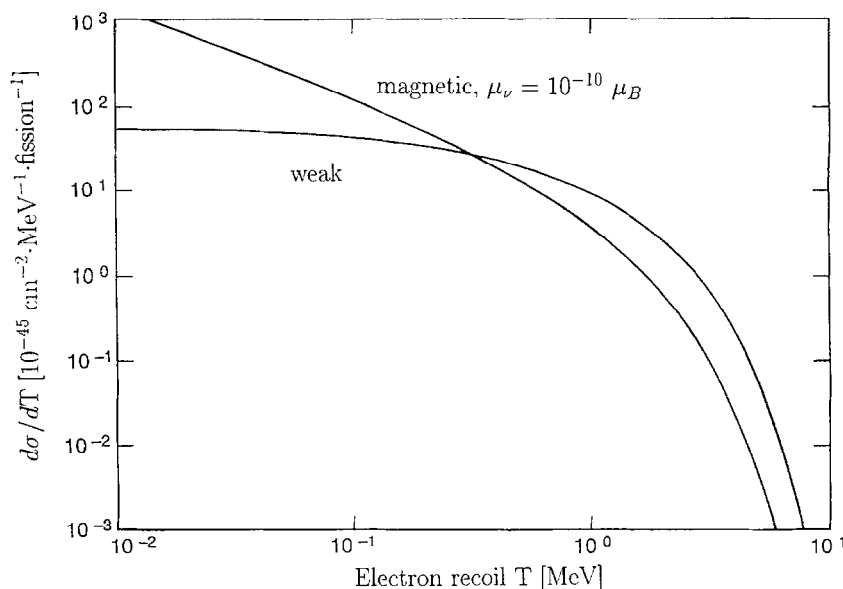
Fig. 1. Expected spectrum of recoil electrons from the reaction $\bar{\nu}_e e^-$ at a $^{235}$U reactor. The contributions of the weak interaction alone and of the magnetic term with $\mu_\nu = 10^{-10}\mu_B$ are shown.

Table 1
Event rate in the Savannah River and Kurtchatov experiments

|  | $T$ (MeV) | Events day$^{-1}$ | | |
|---|---|---|---|---|
|  |  | Reactor on | Reactor off | on–off |
| Savannah | 1.5–3 | 45.1±1.0 | 39.2±0.9 | 5.9±1.4 |
| River | 3–4.5 | 2.4±0.19 | 1.2±0.14 | 1.2±0.25 |
| Kurtchatov | >3.15 | 8.27±0.18 | 7.49±0.31 | 0.78±0.36 |

count in one of the elements of the plastic scintillator with nothing in coincidence. The NaI gave a good anti-Compton efficiency allowing an efficient suppression of the $\gamma$ background. Events from the $\bar{\nu}_e + p \rightarrow e^+ + n$ reaction in the plastic (200 events day$^{-1}$!) were efficiently identified by the detection of the annihilation $\gamma$ rays and/or by the delayed neutron capture signal in the plastic scintillator or in the NaI, and rejected.

The detector was placed at 11.2 m from the core of the reactor operated, at the time, at a power of 1800 MWth, so that the neutrino flux was around $1.9 \times 10^{13}$ cm$^{-2}$ s$^{-1}$. Events were recorded during 64.6 days reactor on and 60.7 days reactor off. The count rates in two bins of electron recoil energy $T$ are shown in Table 1.

The reactor spectrum was poorly known at the time when the experiment was performed. Vogel and Engel [2], using the presently best determination of the reactor spectrum and fixing sin$^2 \theta_W$ to the presently accepted value, find that the measured rates in the two energy bins given above are 1.35 ± 0.4 and 2.0 ± 0.5 times larger than the expected ones.

Taken literally this discrepancy points to a neutrino magnetic moment $\mu_\nu = (2 - 4) \times 10^{-10}\mu_B$.

More recently, a group from the Kurtchatov Institute in Moscow has also successfully observed $\bar{\nu}_e e^-$ scattering [29]. The detector consists of seven identical cells, filled with a $C_6F_6$ based liquid scintillator (103 kg in total), serving as active target material. These cells are viewed by two photomultipliers, one on each side, connected by long light guides to suppress the background from the glass. All the materials chosen are radiochemically very clean, to reduce the background from natural $^{40}$K, $^{232}$Th and $^{238}$U activities, and are essentially hydrogen free, so that there is little background from the reaction $\bar{\nu}_e + p \rightarrow e^+ + n$. The detector is surrounded by various shielding layers to reduce the background from local activities. A plastic scintillator, placed on top of the shieldings, suppresses the background from the cosmics. The neutrino flux, at the detector site, is $3.4 \times 10^{12}$ cm$^{-2}$ s$^{-1}$.

So far, data have been taken for 250 days with reactor on, and 80 days with reactor off. The observed rates, for recoil energies above 3.15 MeV, are 8.27 ± 0.18 day$^{-1}$, respectively 7.49 ± 0.31 day$^{-1}$. The difference gives the reactor associated signal: 0.78 ± 0.36 day$^{-1}$. It is estimated that 0.1 event day$^{-1}$ comes from the background of the reaction $\bar{\nu}_e + p \rightarrow e^+ + n$, the remaining 0.68 ± 0.36 being due to $\bar{\nu}_e e^-$ scattering. This rate is compatible with expectations, obtained with sin $\theta_W = 0.23$, and leads to the limit $\mu_\nu < 2.4 \times 10^{-10}\mu_B$ for the neutrino magnetic moment. This result is not in conflict with the UC Irvine one. A third experiment is in progress at the Rovno reactor [30]. A 75 kg stack of Si detectors is used. But at present the background is overwhelming, and the experiment rather inconclusive.

It clearly appears important to improve by a large factor on these results, and clarify the situation.

## 3. The MUNU experiment

To measure with increased precision $\bar{\nu}_e e^-$ scattering at a reactor we are building a tracking device, a gas time projection chamber (TPC), the drift volume of which serves as electron target. We should thus be able to identify well single electrons originating from inside a predefined fiducial volume. Such a good signature should help in keeping the background down. For instance, multi-Compton events and $c^+-e^-$ pairs inside the drift volume, induced by background gammas, will be rejected. Beta and alpha activities from the walls will be identified as such.

Since we have tracking we will measure not only the recoil energy $T$ of the electron, but also, for the first time, its scattering angle $\varphi_e$, which is given by

$$\cos \varphi_e = \frac{T(E_\nu + m_e)}{p_e E_\nu} \quad (p_e \text{ is the electron momentum}).$$

This has two advantages. First, it will allow a simultaneous measurement of signal plus background events in the forward direction, and background events only in the backward direction. Background can thus be measured on-line, while the reactor is on. This is particularly important in the case of a non optimal signal to background ratio, since the reactor off periods are in general too short to reach good statistical precision.

Second, knowing the electron recoil energy and the scattering angle, we can reconstruct the incoming neutrino energy $E_\nu$. This additional information will result in improved sensitivity. As noted in Ref. [31], the weak interaction part of the cross section at zero angle for $E_\nu = m_e c^2$ cancels exactly. In that kinematical region, corresponding to $T = (2/3)m_e c^2$, the magnetic moment term only contributes. The sensitivity to that term is thus maximal. Of course, the number of events falling in that region is low, and the angular resolution will be limited because of multiple scattering at low energy. Nevertheless, this will provide a useful cross-check, helping in reducing the systematic uncertainties.

Several measures are taken to further reduce the background. First, the absorption length of gammas is non negligible compared to the dimensions of our detector. For instance the probability of a Compton scatter in the fiducial volume with the outcoming gamma escaping out of it is large. To identify such events the central TPC is surrounded by an anti-Compton detector. The anti-Compton was an essential feature of the SRP detector.

Next, to reduce backgrounds from natural activities, the detector is made from radiochemically pure materials. The detector medium, $CF_4$ gas, is hydrogen free, so that the background from $\bar{\nu}_e + p \rightarrow e^+ + n$ scattering will be largely suppressed.

To maximize the count rate the detector will be placed very near one of the Bugey reactors [32]. The exact distance from the core to the center of the detector will be 18.0 m. The reactor power is 2800 MWth, corresponding to about $5 \times 10^{20}$ $\bar{\nu}_e$ s$^{-1}$. The lab has a concrete overburden corresponding to 20 m water equivalent, which gives a modest but welcome suppression of the cosmic rays, and cosmogenic activations.

## 4. The MUNU detector, general description

To summarize the main parts of the detector, shown in Fig. 2, are:
(1) the 1 m$^3$ $CF_4$ TPC as central tracking detector,
(2) the surrounding 50 cm thick anti-Compton scintillation detector, which acts as active shielding,
(3) the lead and polyethylene passive shieldings.

### 4.1. The time projection chamber

The central tracking detector is a 1 m$^3$ time projection chamber (TPC) conceptually similar to the Xe TPC presently operated in the Gotthard underground lab by the Caltech-Neuchâtel-PSI collaboration [33,34]. It is filled with $CF_4$ gas. This gas was chosen for its very high density (3.68 g l$^{-1}$ at 1 bar) and relatively low $Z$, which reduces multiple scattering. The radiation length is $X_0 = 35.9$ g cm$^{-2}$. Also, the cosmogenic activation of C and F is reasonably low, an important consideration since we have only a very small overburden to protect the detector.

The maximal pressure is 5 bar, corresponding to a total number of target electrons of $N_e = 5.29 \times 10^{27}$. The actual operating pressure will be determined by the threshold energy. At 5 bar, electron tracks are long enough for good identification with realistic spatial resolution down to 500 keV. The pressure must be reduced if lower energy electrons are to be investigated. The drift properties of $CF_4$ have been studied by various authors (see Ref. [35] for a summary), and in particular by Schmidt and collaborators in Heidelberg [36]. The drift velocity is very high, ~4 cm μs$^{-1}$ for an electric field of 120 V cm$^{-1}$ bar$^{-1}$. The lateral drift is small and would amount to 2.5 mm after 1 m at the same field strength. The longitudinal drift would be somewhat less, around 2.2 mm.

All these parameters have been obtained from measurements at 1 bar and over a drift distance of a few cm. We have shown however that electrons can be drifted over larger distances in 5 bar of pure $CF_4$ with a mini-TPC prototype. The drift distance is 20 cm and the active diameter 10 cm. To achieve good purity, the gas is circulated continuously through an Oxysorb filter to remove oxygen and a cold trap to remove water and possible freon contaminations. A mean drift length of $L_{drift} = 9^{+9}_{-3}$ m at 5 bar and at 120 V cm$^{-1}$ bar$^{-1}$ was achieved [37]. This is in principle good enough for
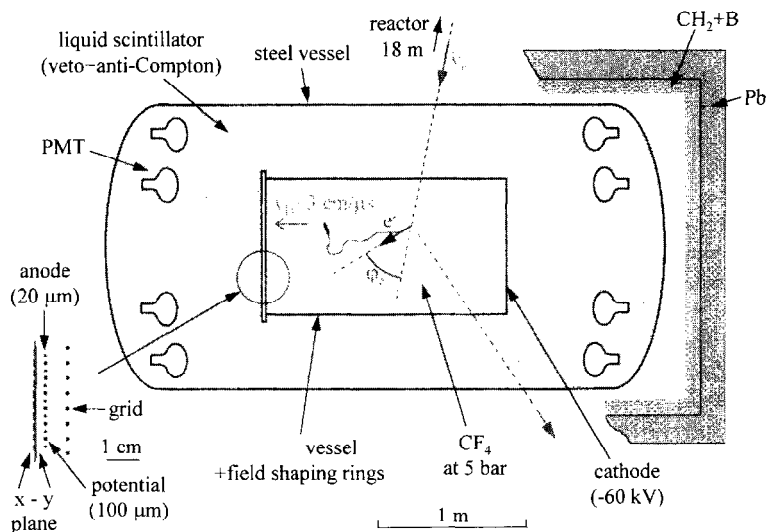
Fig. 2. Layout of the MUNU detector for the study of the $\bar{\nu}_e e^-$ reaction. The central TPC is shown, with the surrounding anti-Compton scintillator, and the various shielding layers. The detector will be installed near one of the Bugey nuclear reactors, at a distance of 18.0 m from the core.

our application. We describe, in Section 7.1, how even larger values have been obtained with the final 160 cm long TPC.

Subsequently, the mini-TPC was modified, and became a scaled down version of the final MUNU TPC [39,40]. It was used to optimize the design of various components. A second version was built, in which the steel vessel was replaced by an acrylic one [41]. It served to verify the possibility of operating a TPC with an acrylic vessel, as well as the compatibility of $CF_4$ with acrylic.

Measurements of the drift velocity from the pulse length of through-going cosmic muons were also performed with the mini-TPC. The results are in good agreement with previous determinations [35]. In addition spectra obtained with an $^{113}$Sn electron conversion source were used to determine the energy resolution. At 5 bar and with a drift field of 120 V cm$^{-1}$ bar$^{-1}$ it turned out to be better than 20% FWHM at 370 keV.

The 1 m$^3$ TPC is shown in Fig. 2. The $CF_4$ gas at pressure up to 5 bar is contained in a cylindrical acrylic vessel of inner diameter 90 cm and 160 cm long. The drift volume is delimited by a cathode on one end of the vessel, and a grid on the other one.

The cathode is held at negative high voltage. Field shaping rings made from copper stripes, 2 mm wide and 0.5 mm thick, are wrapped around the acrylic vessel, with a 1.5 cm spacing. They are tensioned with small springs and interconnected with high voltage 10 M$\Omega$ resistors. Still with resistors, the first ring is connected to the cathode and the last one to the grid, in such a way that cathode, shaping rings and grid define an homogeneous drift field inside the acrylic vessel. With this design, the $CF_4$ volume is active over its entire diameter.

Behind the grid is an anode plane. The inner diameter of the frame is 90 cm. All anode wires are connected together to give the energy signal. The following plane contains two sets of isolated perpendicular strips to pick up the induced signals. The pitch, 3.5 mm, is well adapted to the lateral drift in $CF_4$. This $x-y$ plane provides the spatial information along the $x$- and $y$-axis in the anode plane. The $x-y$ plane is kept at ground potential, while the anode plane is at a positive high voltage large enough to have good amplification around the anode wires. This way the number of high voltage feed-throughs is minimal, which is important for the low background environment. The third coordinate, along the drift field ($z$) is determined from the time evolution of the signals. This allows a determination relative to the point of the track closest to the grid. The tracks obtained with the mini-TPC, equipped with a similar anode and $x-y$ plane, showed that the spatial resolution is of order $\sigma \simeq 1$ mm in $x$, $y$ and $z$ direction.

To fully exploit the information provided by the TPC, we have developed a read-out electronics with 8 bit flash ADC's for the anode and each $x$ or $y$ strip. The sampling speed is 40 ns, and the memory size is 1024 words for each channel [42]. The same system will be used for the photomultipliers.

### 4.2. The anti-Compton scintillator and the shielding

The acrylic vessel is immersed in a stainless-steel tank filled with a mineral oil based liquid scintillator provided by Nuclear Entreprises. The attenuation length was measured to be 8 m at 430 nm wavelength. The liquid scintillator serves to veto the cosmic muons and as anti-Compton detector. It is viewed by 48 hemispherical photomultipliers, 24 on each

lid, of 20 cm diameter. The photomultipliers, bought from EMI, are made with low activity glass. They are immersed in the scintillator, along with their bases, and held in place by a polyethylene structure. On the cathode side they are shielded against the electric field generated by the high voltage by a screen made with 100 μm diameter widely spaced tungsten wires.

The photomultipliers will trigger at the one photo-electron level. With this, and considering the scintillator thickness which is 50 cm, the anti-Compton efficiency is about 98% for $\gamma$ energies above 100 keV.

The liquid scintillator and the steel vessel also serve as low activity shielding. In addition, outside the steel vessel, there are 8 cm of polyethylene to absorb neutrons entering the detector. The first and the last cm are loaded with boron. Still further out are 15 cm of lead, in the form of bricks and pellets held in place by a steel structure, to further reduce gamma activities from outside.

## 5. Event and background rate

The expected $\bar{v}_e e^-$ rates at 18 m from the 2800 MWth Bugey reactor have been calculated using Eq. (1), for $\mu_v = 0$, taking into account weak interaction only with $\sin^2\theta_W = 0.2325$, and for $\mu_v = 10^{-10}\mu_B$, and are given in Table 2. The acceptance for fully contained electrons was estimated by Monte-Carlo simulation using the GEANT code [43].

The total event rate for $T > 0.5$ MeV is 9.5 day$^{-1}$ with no magnetic moment, and 13.4 day$^{-1}$ for $\mu_v = 10^{-10}\mu_B$. These rates have to be compared to background rates, which are estimated in the following.

The background rate was calculated assuming a 100 keV threshold for the anti-Compton rejection and a forward angle selection. The threshold in the TPC was set to 500 keV. The simulations were performed with the codes GEANT and GAMTRACK [44]. The main components of the background are due to the cosmics and to natural activities of the materials.

The Bugey lab has a large overburden of steel, concrete and water corresponding to about 20 m water equivalent. Neutrons produced in the atmosphere are practically entirely eliminated, while the muon flux was measured to be 32 m$^{-2}$ s$^{-1}$. Some $\mu^-$'s stop in the gas and are captured in nuclei, leading to a cosmogenic $\beta$ activity [45]. But this only contributes a fraction of an event per day (Table 3) to the background rate. Neutrons however are also created in these $\mu^-$ captures. These neutrons can then be captured in hydrogen nuclei in the scintillator or in iron and lead nuclei in the shielding, producing gamma rays (Table 4). These $\gamma$'s in turn produce Compton electrons, which lead to a non negligible background. In all, the background rate of cosmic origin is estimated to be about 2 events per day.

The other important component is that from natural activ-

Table 2
Expected $\bar{v}_e e^-$ event rates in MUNU

| $T$ (MeV) | Acceptance (Contained) | $\bar{v}_e e^-$ Events day$^{-1}$ | |
|---|---|---|---|
| | | $\mu_v = 0$ | $\mu_v = 10^{-10}$ |
| 0.5–1 | 0.85 | 5.3 | 8.1 |
| > 1 | 0.65 | 4.2 | 5.3 |

Table 3
Background induced by $\mu^-$ capture in the CF$_4$ gas

| Interaction | Isotope produced | Events day$^{-1}$ |
|---|---|---|
| $\mu^- - {}^{12}C$ | ${}^{12}B$ | $3.3 \times 10^{-2}$ |
| $\mu^- - {}^{19}F$ | ${}^{19}O$ | $6.5 \times 10^{-2}$ |
| | ${}^{18}N$ | $4.2 \times 10^{-3}$ |
| Total | | 0.1 |

ities. Great care was taken to select radiochemically clean components for the construction of the detector. For the materials entering in large quantity, near the fiducial volume, namely the acrylic for the vessel and the mineral oil for the scintillator, neutron activitation measurements have been performed [46]. The scintillator itself was also tested after the addition of the pseudocumene and the wavelength shifters to the oil. In these measurements sensitivities of order $10^{-13}$ g g$^{-1}$ to ${}^{40}K$ contaminations, and $10^{-12}$ g g$^{-1}$ to ${}^{232}Th$ and ${}^{238}U$ contaminations are achieved.

Gamma activity measurements were also made using various low background Ge detectors. The facilities of the Gran Sasso underground laboratory [47] and of the Fréjus underground laboratory [48] were used in specific cases. In addition heavy use was made of our own Ge detectors in the Vue-des-Alpes underground lab and in the laboratoire des basses activités in Grenoble. The sensitivity to ${}^{232}Th$ and ${}^{238}U$ contaminations is only of order $10^{-10}$ g g$^{-1}$, assuming secular equilibrium, but other nuclides such as ${}^{137}Cs$ or ${}^{60}Co$ can be searched for. All components entering in smaller quantities in the construction of the central TPC and of the anti-Compton detector were selected by gamma spectrometry only. This includes the materials to fabricate the anode, grid and $x$–$y$ planes, the flat signal cables with their connectors, the components of the resistor chain of the TPC, the field shaping rings, the pseudocumene and the wavelength shifters, the bases of the photomultipliers and the photomultipliers themselves.

Table 5 lists the measured activities of various materials or components used for the MUNU detector. For complex components the numbers quoted are the weighted average values of the activities measured for each subcomponent.

In all the background rate from natural activities, essentially due to Compton electrons induced by the $\gamma$ activity, is estimated to be about 4 events per day.

C. Amsler et al. / Nucl. Instr. and Meth. in Phys. Res. A 396 (1997) 115–129

121

Table 4
Major backgrounds induced by neutrons in materials of the MUNU detector

| Neutron capture | | Events day$^{-1}$ | | | Events day$^{-1}$ |
| | | Neutron creation site | | | Total |
| Medium | Type | Liquid + acrylic | Steel vessel | Shielding | |
| --- | --- | --- | --- | --- | --- |
| Gas | $^{19}F(n, x)X^*$ | 0.038 | 0.006 | 0.018 | 0.06 |
| Liquid + acrylic | $H(n, \gamma)^2H$ | 0.18 | 0.25 | 0.36 | 0.79 |
| Steel vessel | $^{56}Fe(n, \gamma)^{57}Fe$ | | 0.17 | 0.42 | 0.59 |
| Shielding | $H(n, \gamma)^2H$ | | 0.01 | 0.16 | 0.17 |
| | $Pb, Fe(n, \gamma)X$ | | | 0.07 | 0.07 |

Table 5
Measured radioactive contamination of various materials or components used for the construction of the MUNU detector

| Medium | Contaminations | | | |
| | A | unit $g\,g^{-1}$ | Meas. | Upper limit |
| --- | --- | --- | --- | --- |
| Acrylic | U | $10^{-12}$ | | 3.00 |
| vessel | Th | $10^{-12}$ | | 4.00 |
| | K | $10^{-7}$ | 2.00 | |
| Steel | U | $10^{-9}$ | 0.03 | 0.87 |
| vessel | Th | $10^{-8}$ | 0.18 | 0.34 |
| | Cs | $10^{-18}$ | 0.42 | 0.93 |
| | Co | $10^{-19}$ | 0.76 | 1.08 |
| | K | $10^{-5}$ | 0.14 | 0.14 |
| P.M.T | U | $10^{-7}$ | 0.41 | |
| | Th | $10^{-7}$ | 0.49 | |
| | Cs | $10^{-18}$ | | 2.00 |
| | Co | $10^{-19}$ | 0.56 | |
| | K | $10^{-4}$ | 0.85 | |
| Liquid | U | $10^{-12}$ | | 3.00 |
| scint. | Th | $10^{-12}$ | | 3.00 |
| | Cs | $10^{-20}$ | 0.20 | |
| | K | $10^{-8}$ | 0.30 | |

The background generated by $\bar{\nu}_e p \rightarrow e^+ n$ charged current interactions in the acrylic and the liquid scintillator is negligible (Table 6). The total background is thus estimated to be of order of 6 events per day, with a threshold of 500 keV in the TPC.

### 5.1. Signal versus background, capability of the experiment

The total background rate which will be measured during two reactor-off periods ($\sim 2$ months) is thus expected to be smaller than the signal rates for $T > 0.5$ MeV (Table 2). We remind that the background will be also determined with better precision from the event rate in the backward half sphere and subtracted. The isotropy of the background could be verified by relaxing some of the selection conditions. Considering the signal rates at 18.0 m in Table 2,

Table 6
Calculated background rate from the reaction $\bar{\nu}_e - p$ in the liquid scintillator and the acrylic

| Neutron interaction | | Events day$^{-1}$ |
| Medium | Type | |
| --- | --- | --- |
| Gas | $^{19}F(n, \gamma)^{20}F$ | $2.13 \times 10^{-3}$ |
| Liquid + acrylic | | |
| | $H(n, \gamma)^2H$ | 0.251 |
| Total | | 0.253 |

a statistical error less than 3% should be achievable in the bin $0.5 < T < 1$ MeV in one year of measuring time. Combined with a systematic error of 5%, essentially from the reactor spectrum (3%), reactor power and burn-up (2%) and
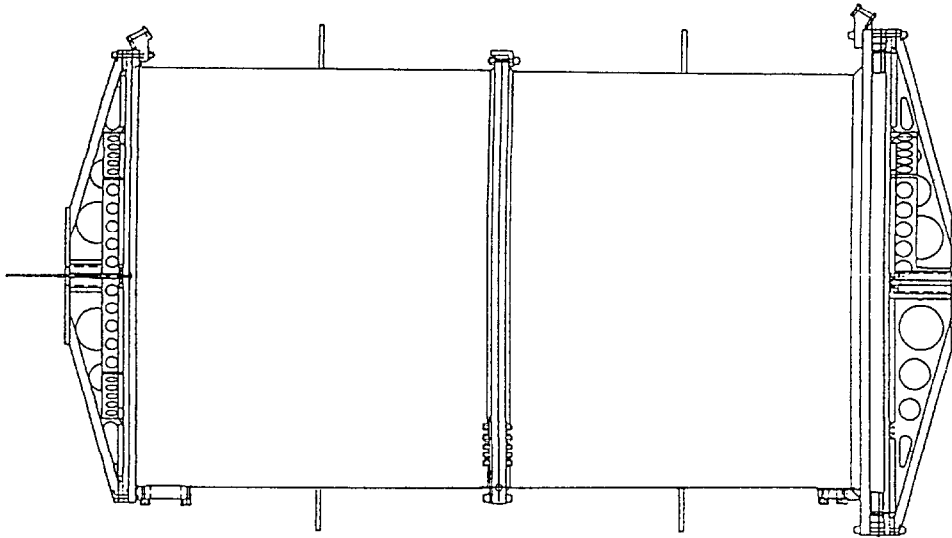
Fig. 3. The acrylic vessel. The cathode side is on the left. The flanges to connect the gas in and gas out pipes are shown at the bottom of the cylinder.

detection efficiency (3%), this leads to a sensitivity to the magnetic moment of the neutrino of

$$\mu_\nu \sim 3 \times 10^{-11} \mu_B,$$

a factor 10 better than in previous experiments. This sensitivity is mainly limited by the systematic uncertainties and changes only slowly as a function of the signal versus background ratio. The limit value on $\mu_\nu$ would be around $4 \times 10^{-11} \mu_B$ if the background is increased by a factor of 4.

The signal rate for the bin $T > 1$ MeV (4.2 day$^{-1}$) from weak interaction alone is equivalent to that in the lower energy $0.5 < T < 1$ MeV bin (5.3 day$^{-1}$), while the contribution from the magnetic moment term is more than a factor of two lower. Using the ratio of the rates in these two energy bins, we will be able to cross check with reduced systematics the contribution of the magnetic moment. This requires however larger statistics, and a significantly longer data taking time. Also, as explained in Section 3, the study of the angular distribution of the recoil electrons will provide a useful cross-check, allowing to reduce systematic uncertainties. Our detector is the first one to measure not only the electron kinetic energy, but also the scattering angle.

Depending on the actual background, the threshold may be lowered, say down to 300–350 keV. To have tracks of reasonable length, it will be necessary to lower the pressure at the same time, say to 3 bar. The event rate should remain essentially unchanged since the electron recoil spectrum peaks at low energy. A sensitivity around $2 \times 10^{-11} \mu_B$ seems then achievable.

We would also like to add that a change of $\pm 5\%$ in $\sin^2 \theta_W$ changes the event rate by 4.3% in the energy bin 0.5–1 MeV, and by 5.8% above 1 MeV. A 5% determination of $\sin^2 \theta_W$ appears thus possible in our experiment, assuming a small

magnetic moment. This accuracy is rather good, considering that we are dealing with a purely leptonic process. It is comparable to that achieved by the CHARM II collaboration in the study of $\nu_\mu e$ scattering [49].

## 6. Detailed description of the MUNU time projection chamber

Having given a general description of the experiment, we now present in more details the central component of the MUNU detector, namely the time projection chamber with its gas handling system. Results of first tests are presented, including a new measurement of the attenuation length in the CF$_4$ fill gas. These demonstrate the feasibility of the experiment.

### 6.1. The acrylic vessel

The acrylic vessel is shown in Fig. 3. It is made with as little material as possible to minimize the inactive volume. All the parts are made from acrylic selected for low radioactivity. The vessel is of cylindrical shape, with an inner diameter of 90 cm, and a length of 162 cm, and is closed with two lids. The central cylinder is split up into two pieces small enough to go through the entrance of the laboratory under the reactor. Acrylic glue was used to assemble all the parts of the cylinders and the lids.

The wall thickness of the cylinders is only 0.5 cm. To give more strength, a reinforcing ring has been glued in the middle of each piece, in addition to the flanges at both ends. These are used to bolt the two cylinders together, and the lids to the cylinders. Delrin bolts were chosen. The two lids
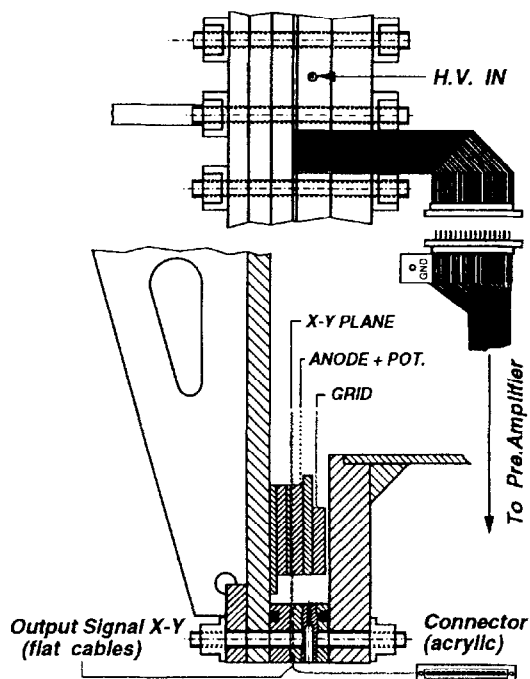
Fig. 4. The frames of the anode and *x–y* planes on the lid of the acrylic vessel.

are 1.2 cm thick plates reinforced with an octagonal structure. The seals between the two cylinders and between the cylinders and the lids are made with Viton O-rings (Fig. 4). On one side, a spacer ring was squeezed between the lid and the flange, to make room for the frames of the read-out planes (anode and *x–y*, Section 6.3).

The total weight of the acrylic vessel is ∼100 kg. It was tested that the acrylic vessel can stand a pressure difference between inside and outside of up to ±100 mbar, more than the difference in hydrostatic pressure between top and bottom, when in the steel vessel filled with liquid scintillator.

The acrylic vessel is attached to the large steel vessel by acrylic bars. Most are on the top side, arranged radially: three at each end, and five at the center. An additional plate is screwed to the bottom center. These pieces are strong enough to counterbalance the buoyancy. One additional advantage of acrylic for these pieces is that it transmits the scintillation light.

To avoid excessive pollution of the $CF_4$ gas the vessel must be thoroughly outgassed before filling. Before pumping for the first time the vessel was cleaned with deionized water and then with pure hexane. We then had to pump for a rather long period (∼4 weeks) keeping the vessel at a temperature of 60°C in order to reach a residual pressure of $10^{-5}$ mbar inside the chamber.

To reduce mechanical stress during this initial pumping, the acrylic chamber was placed inside a cylindrical stainless steel vessel similar to the one to be used in Bugey but of smaller size (inner diameter 120 cm). The steel vessel was

evacuated at the same time as the acrylic vessel. For convenience reasons all of the early tests of the TPC described in this paper were performed in that configuration.

### 6.2. Gas handling and purification

An active pressure equalizing system maintains the same pressure, within at most 20 mbar, inside the two vessels, not only while pumping, but also during all subsequent operations: filling with $CF_4$ gas to a given pressure, measurements at that pressure, gas recuperation.

The active pressure equalizing system measures the pressures in both vessels with electromechanical gauges, as well as the pressure difference with a third gauge. While evacuating it adjusts the pressures by opening and closing electromechanical valves on the steel vessel and acrylic vessel vacuum lines. While filling, it activates valves on the $CF_4$ line for the acrylic vessel, and a nitrogen line to pressurize the steel vessel. In normal mode, it maintains the pressures constant by activating not only the $CF_4$ and nitrogen inlet valves, but also valves to release these gases.

A scheme has been devised to recuperate the $CF_4$ gas before opening the detector for servicing. The bottom part of the gas cylinder for $CF_4$ storage is immersed in liquid nitrogen, and connected to the acrylic vessel, so that $CF_4$ starts condensating. During the entire procedure, the gas pressure equalizing system controls the pressure difference between the steel vessel and the acrylic vessel. When the pressure in the acrylic vessel has dropped below 100 mbar, and most of the $CF_4$ has been recuperated, the cylinder is isolated. Dry nitrogen is introduced into the acrylic vessel before opening, to avoid water adsorption on the walls. This reduces considerably the time required to achieve good vacuum in the acrylic vessel at the next pumping.

The same pressure equalizing system will be used in Bugey to regulate the pressure on the $CF_4$ gas inside the acrylic vessel and on a nitrogen blanket for the liquid scintillator inside the steel vessel.

The gas introduced into the chamber is the cleanest $CF_4$ commercially available (99.999% pure). It is circulated continuously through an Oxysorb filter from Messer Griesheim to remove oxygen and water, and through a cold trap to remove possible freon contaminations. The circulation pump is a two metal bellows pump which can work at 7 bar pressure and maintain a flux up to 1500 l/h. The cold trap consists of a steel tube spiral, through which $CF_4$ is flowing, immersed in an ethanol bath kept at a constant temperature just above the boiling point of $CF_4$, −95°C, at 5 bar. The cooling power of the trap is 70 W at −95°C.

### 6.3. The drift field, the anode and x–y planes

The cathode, a plain 0.2 mm thick copper plate, is screwed to one of the lids of the acrylic vessel. The frames for the *x–y* plane, anode plane and grid are screwed to the other lid. The cathode, grid and field shaping rings define a
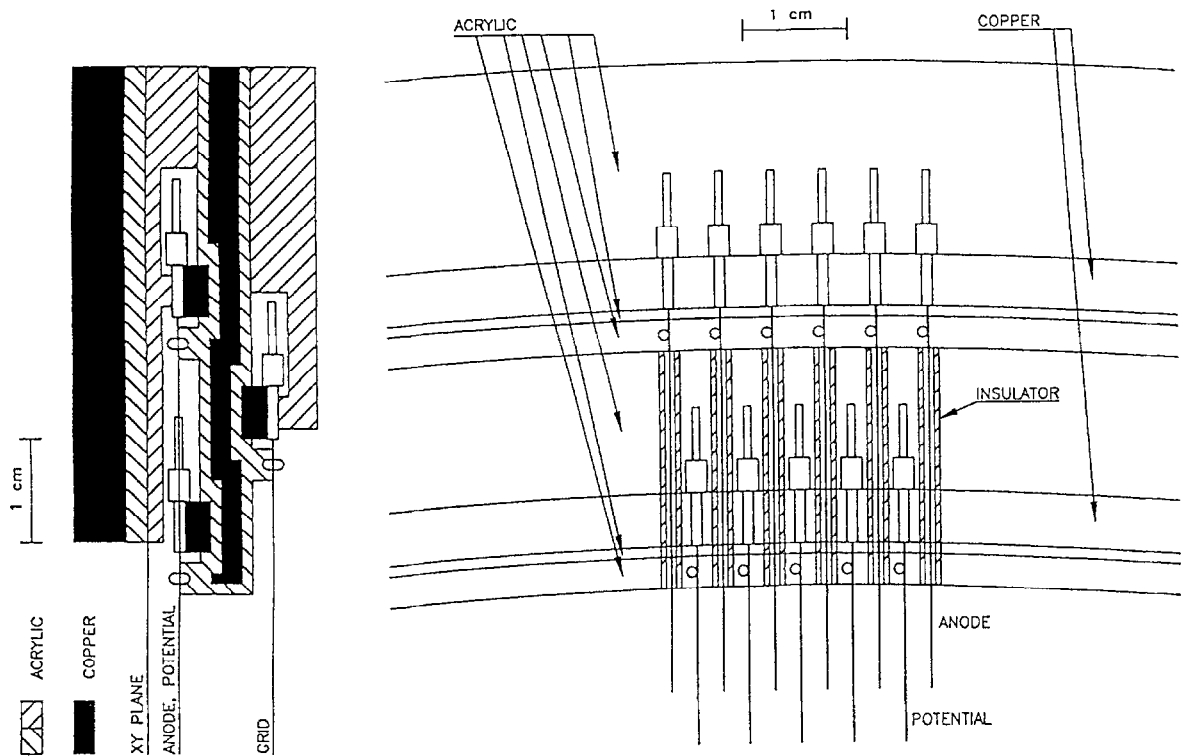
Fig. 5. The frame of the wire planes for the MUNU TPC.

homogeneous electric drift field in the entire volume of the vessel. The cathode is maintained at a negative high voltage of up to $-80\,\mathrm{kV}$. The connection is made at the center, with a cable traversing axially the steel vessel. The grid is held at a negative potential, as described later. Cathode and grid are connected with a resistor chain on the outside of the acrylic vessel. After each resistor $(10\,\mathrm{M\Omega})$, contact is made with a field shaping ring. The spacing is 15 mm. The rings themselves are made from phosphorous bronze wires $(\varnothing\ 0.7\,\mathrm{mm}, 94\%$ copper and tin) and tensioned with springs made from the same material around the acrylic vessel.

The anode and grid planes are mounted on both sides of one single ring, of 90 cm inner diameter, matching the active diameter of the chamber (see Fig. 5). The core is a copper ring, providing the mechanical stiffness. For electrical insulation it is sandwiched between two acrylic rings glued one on the grid side, the other one on the anode side.

The anode plane contains the anode wires themselves, with a spacing of 4.95 mm, alternating with potential wires for electrical separation. The anode wires $(\varnothing\ 20\,\mu\mathrm{m})$ and the potential wires $(\varnothing\ 100\,\mu\mathrm{m})$ are made from pure tungsten. The anode wires are mounted on a narrow copper ring, itself glued on the acrylic ring. The potential wires are attached to a second copper ring, identical to the first one, except for the smaller diameter. The wires are crimped in small hollow copper needles, of inner diameter $200\,\mu\mathrm{m}$, held in

place in grooves machined in the copper rings. For long-term stability the anode wires are glued to the needles at the rear end by a droplet of acrylic glue. The mechanical tension is 60 g for the anode wires, just beyond the limit of elasticity, and 200 g for the potential wires. The electrical contact between the anode wires, or the potential wires, is provided by the copper rings.

The lateral position of the wires is defined to within $10\,\mu\mathrm{m}$ by small pins against which they are pushing. The anode wires are isolated from the potential wires by U-shaped Delrin insulators on the frame, and over a distance of roughly 1 cm beyond it.

The grid wires are also made from plain tungsten and have a diameter of $100\,\mu\mathrm{m}$. They are mounted in a similar way, the grid wires being perpendicular to the anode wires. The distance between the grid and anode planes is 8.5 mm. The design chosen ensures good mechanical precision, in particular for the anode and potential wires, which is important for the uniformity of the gain.

The $x$–$y$ plane is a $125\,\mu\mathrm{m}$ thick mylar foil covered on both sides with a $35\,\mu\mathrm{m}$ copper film. The strips, $x$ on one side and $y$ on the opposite one, are made by etching. The strips are diagonal with respect to the anode and grid wires. To have a uniform lattice the spacing between strips is 3.5 mm, which is that between anode wires, 4.95 mm, divided by $\sqrt{2}$. The pattern (Fig. 6) is such that the screening between
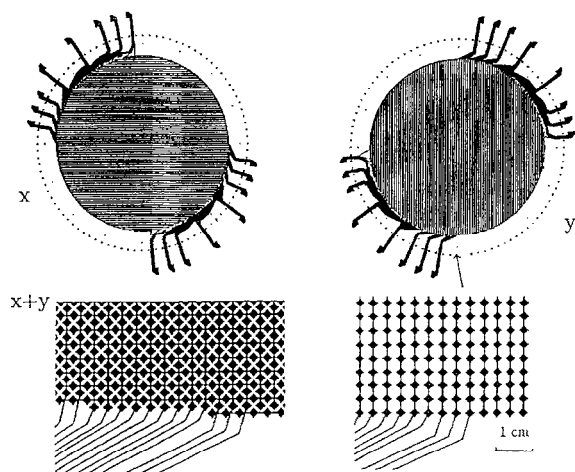
Fig. 6. Schematics of the x–y plane.



Fig. 7. Arrangement of the flat cables for the x and y strips. The steel vessel and the acrylic vessel are shown.

x and y strips is minimal. The foil is stretched and glued on a 1 mm thick acrylic ring, for electrical insulation, itself glued on a copper ring, for stiffness. This frame is screwed, along with the frame for the anode and grid planes on the lid of the acrylic vessel (Fig. 4). The x–y plane is located 3 mm behind the anode plane (Fig. 5).

In total, there are 512 strips, 256 x and 256 y. At the edge, the mylar foil extends into 32 flat cables. The strips are brought together, in groups of 16, which are led into the 32 flat cables. The flat cables leave the lid of the acrylic vessel through slots in the edge of the spacer ring. These slots are sealed with acrylic glue. These cables are crimped to home-made low activity connectors outside the vessel, connected in turn to 2 m long flat cables made in a similar way. These long cables are, however, covered with a thin insulating layer. They carry 16 signal leads on one side and a ground strip on the other one. They are bundled in 4 groups of 8 which go to 4 feed-throughs in the steel vessel, through a labyrinth in the shielding, to preamplifiers located outside the Pb shielding (Fig. 7). This arrangement minimizes the absorption of scintillation light by the cables. Also the detector is shielded against radio-activities from the preamplifiers. To minimize the electronic noise, it was necessary to shield electrically the cables along the portion outside the steel vessel with great care.

To avoid soldering all electrical connections are made with connectors, crimps, or screws. Solder is a problem from the point of view of radiopurity, as it contains $^{210}$Pb. All the glueing was done with acrylic glue, which was found to be sufficiently clean.

In normal operation the x and y strips are maintained at ground potential at the input of the preamplifiers. The anode wires are maintained at a positive potential sufficient for reasonable amplification. The potential wires are held at ground potential, or at a positive potential significantly lower than that of the anode. Since the distance from the grid to the anode is larger than that from the anode to the
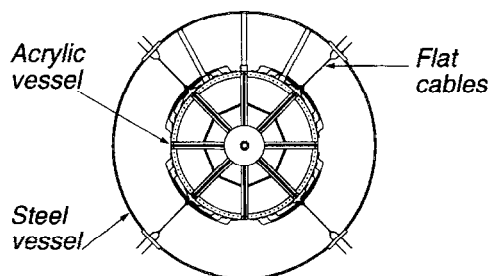
x–y plane the grid wires are held at a negative potential. Specific potential configurations are given in Section 7.2.

Each x and y strip has its own preamplifier, operated in current–voltage mode ($270 \, \text{mV} \, \mu\text{A}^{-1}$). The design is based around a LeCroy TRA1000 circuit. The rise time of the signals at the output of the preamplifier is around 200 ns. In normal operation, the preamplifier signals are sampled every 40 ns with 8 bit FADC's (Struck DL350 system). The input range extends from 0 to −600 mV. The response function is non-linear to increase the amplitude resolution for small signals. A 1024 word memory is associated to each channel. The anode wires, coupled together by the copper ring, are connected to a single similar preamplifier, sampled in the same way. This additional information makes it often easier to identify ends of tracks from the increased $dE/dx$, and to single out $\alpha$ particles. event is best determined by integrating the anode signal.

## 7. Test measurements

### 7.1. Anode signals and attenuation length measurements

In a first series of tests we verified that our gas handling system works satisfactorily. For these, as mentioned earlier, the acrylic vessel was mounted in a steel vessel similar to that to be used in Bugey, but of smaller size. The acrylic vessel was resting horizontally on spacers on the bottom of the steel vessel. The connections to the gas circulation system and to the pressure equalization system were the same as in the final design. The steel vessel was not filled with liquid scintillator, however, but with nitrogen, at the pressure determined by the gas pressure equalization system, slightly below that in the acrylic vessel.

The acrylic vessel was equipped with the cathode, the field shaping rings, the grid and the anode. Only 16 x and 16 y strips were connected to flat cables and brought out of the steel vessel. The other ones were grounded outside the acrylic vessel.

We looked at anode signals induced by cosmic muons to verify that the gas purification system brings the gas to a level of purity sufficient to drift electrons. Measurements
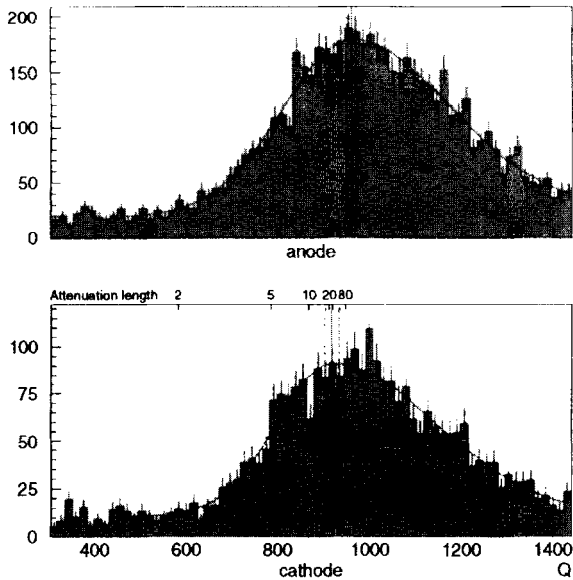
Fig. 8. Measured energy deposition of nearly vertical cosmic muons crossing the TPC at 30 cm from the anode (top) and 30 cm from the cathode (bottom), at 3 bar and with a drift field of 50 V cm$^{-1}$ bar$^{-1}$. The fitted peak position is indicated. The upper horizontal axis of the bottom spectrum shows the attenuation length for a given peak position.

were performed at 1 and 3 bar, with a drift field ranging from 50 to 80 V cm$^{-1}$ bar$^{-1}$. At the latter field strength the drift velocity was 3.2 cm μs$^{-1}$ bar$^{-1}$.

Two plastic scintillators covering an area of $40 \times 40$ cm$^2$ were placed one on top of the steel vessel, the other one just below. They were used as a telescope to tag muons entering nearly vertically into the detector. Data were taken with the telescope axis at a distance of 30 cm from the anode, and 30 cm from the cathode. Signals induced by these muons are relatively short since the tracks are nearly perpendicular to the drift field. After the preamplifier, they were shaped in a spectroscopy amplifier (integration and differentiation constants 5 μs), and analyzed in a multi-channel analyzer. They correspond to an energy deposition of 480 keV at 1 bar, and 1.5 MeV at 3 bar. They give rise to the peaks shown in Fig. 8.

One sees that the peaks for the two telescope settings are essentially in the same position. The fitted peak positions with their uncertainties are indicated. Taking into account that the difference in the drift distances is 1 m, one concludes that the mean atenuation length is

$$L_{drift} = 22^{+14}_{-6} \text{ m} \quad \text{at 3 bar}$$

with a drift field of 50 V cm$^{-1}$ bar$^{-1}$. This is largely sufficient for MUNU.

## 7.2. The x–y signals

The current in the induced x–y signals is roughly 5 times lower than in the anode signals. The anode high voltage must be adjusted so that they exceed, comfortably, the noise level. Using the connected strips we looked at the x and y signals induced by minimum ionizing nearly vertical cosmic muons tagged by the telescope. For these measurements the telescope was placed in the middle of the TPC, at equal distance from the anode and the cathode.

Reasonably large signals, namely of order 5–10 mV, were observed with a digital oscilloscope at anode and grid voltages of +1850 V, respectively, −3330 V at 1 bar, and +2570 V, respectively, −4625 V at 3 bar, the potential wires being maintained at ground potential. The drift field was 60 V cm$^{-1}$ bar$^{-1}$. This signal amplitude is adequate, since the rms noise is less than 2 mV. Examples are shown in Fig. 9. These output voltages correspond to an input current of around 70 000 e$^-$/300 ns for the signal, and 14 000 e$^-$ for the noise.

Next the signals were analyzed with the final read-out system, the preamplifiers feeding the DL350 FADC's. In these measurements, performed at 3 bar, the anode and grid voltages were raised to +2700 V, respectively, −4860 V. The x–y plane was oriented so that the x strips were almost vertical, thus measuring the horizontal coordinate. As a consequence, the ionization density is high along the x strips, and close to the minimum on the y strips. This is clearly visible in the example shown in Fig. 10, the measured charge density is higher in the x–z projection of the track than in the y–z projection. But good signal to noise ratio is achieved even for the most unfavorable projection.

To estimate the local spatial resolution, we fitted a straight line through the y–z projection. We then evaluated the average mean squared deviation of the fitted signal centroid on each strip to the line. The square root gives the standard deviation

$$\sigma = 1.6 \text{ mm}$$

which can be considered a measure of the spatial resolution at 3 bar. More elaborate algorithms, which we are developing, will be necessary to fully exploit the spatial resolution when reconstructing tracks of low energy electrons, which curl more than those from through going cosmic muons.

## 7.3. Energy resolution

Measurements were also made of the energy resolution with an $^{241}$Am source emitting 59.5 keV γ-rays. For convenience reasons these measurements were carried out with the actual anode and x–y planes in a shorter steel vessel. The drift volume was defined by a cage supporting field shaping rings and a cathode, the depth of the drift volume being 13 cm. The source was placed outside the steel vessel, on the side of the drift volume. Measurements were made at 3 and 5 bar.
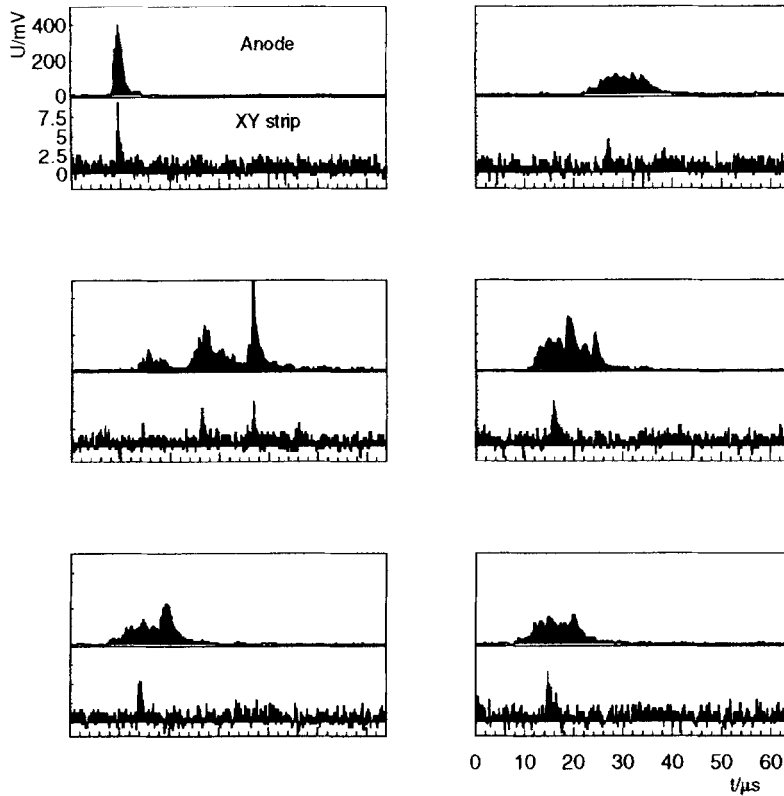
Fig. 9. Examples of signals on the anode and an $x$ strip, measuring the horizontal coordinate, induced by nearly vertical cosmic muons, seen at the output of the preamplifiers.

In these measurements a field configuration calculated with the GARFIELD code [50] was used, the ratio of anode to grid voltage being $-1.75$. This symmetrizes the electric field with respect to the anode plane, and thus reduces the mechanical stress on the anode wires. As a consequence the sagitta of the anode wires is minimal, and the gain uniformity is improved. The actual anode voltages were 3350 and 4450 V at 3, respectively, 5 bar. The voltage on the potential wires was raised to 400, respectively, 500 V, to avoid discharges between the anode and potential wires. The anode signals were processed as described in Section 7.1. Since the signals are short, the integration and differentiation constants of the shaping spectroscopy amplifier were set to 1, respectively, 1.5 μs. The spectra obtained at 3 and 5 bar of $CF_4$ are shown in Fig. 11.

The full absorption peak is clearly visible. Fitting a Gaussian to the peaks yields an energy resolution (FWHM) of 28 keV corresponding to 48% FWHM at 3 bar. At 5 bar it is 34 keV, equivalent to 58%. The contribution of the electronics noise is of order 6 keV and is thus negligible. The energy resolution was found to change only little in additional measurements performed at different anode voltages.

Assuming that the energy resolution scales with the inverse square root of the energy, as it does in the Xe TPC operated in the Gotthard lab [34], we expect a resolution of order 20% FWHM at 500 keV. This is in rough agreement with what was observed in that energy range with the mini-TPC (Section 4.1), and is adequate for the MUNU experiment.

## 8. Conclusion

We have presented MUNU, a new detector for the detailed study of $\bar{\nu}_e e^-$ scattering at a nuclear reactor. The central component is a 1 m³ time projection filled with $CF_4$ gas at pressures up to 5 bar. It is surrounded by an anti-Compton scintillator to reduce the background. Radiochemically clean components have been selected for all components. The detector is presently being set up near the Bugey reactor.

First results obtained with the time projection chamber have been presented. A mean attenuation length of $L_{drift} = 22^{+14}_{-6}$ m at 3 bar with a drift field of 50 V cm$^{-1}$ bar$^{-1}$ was achieved. Under the same conditions the spatial
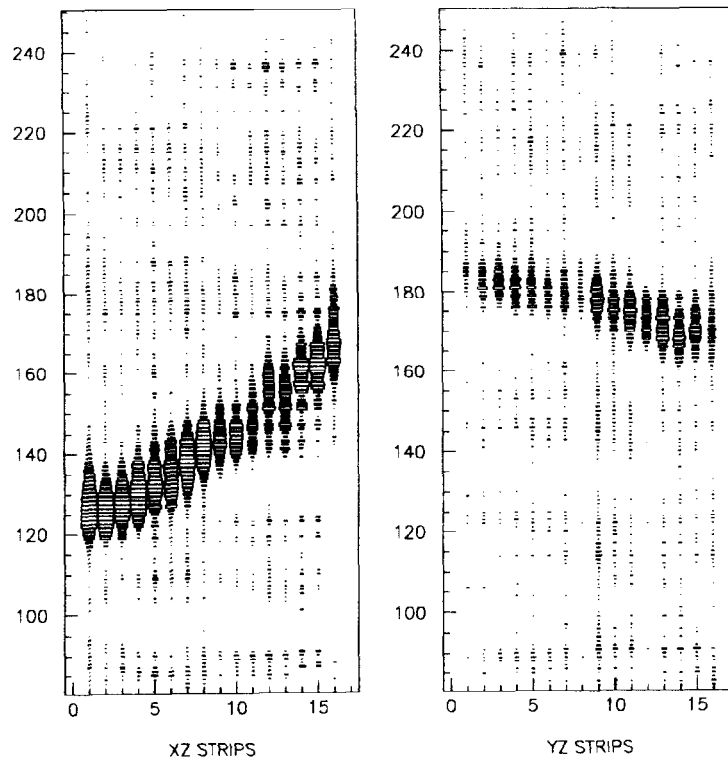
Fig. 10. Cosmic muon tracks (xz and yz projections) observed with the central 16×16 central x and y strips at 3 bar. The distance between two strips (horizontal axis) is 3.5 mm. The vertical z axis is such that 20 channels correspond to 2.56 cm. The area of the rectangles is proportional to the current measured on a strip. Only part of the track is in the overlap region of the x and y strips, so that both projections are displaced along the z-axis.
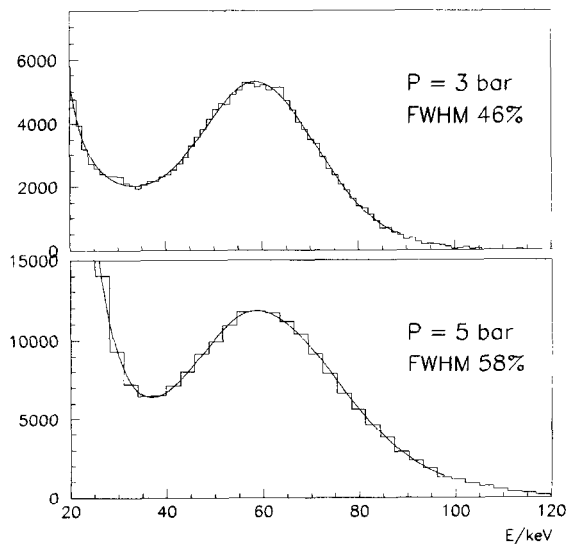


Fig. 11. Energy spectra obtained with the actual anode and x–y plane in the short-time projection chamber (see text) exposed to an $^{241}$Am source, at 3 and 5 bar $CF_4$. The anode voltages were 3350 and 4450 V at 3, respectively, 5 bar.

resolution was determined to be $\sigma = 1.6$ mm. This is largely sufficient for MUNU.

Beyond demonstrating the feasibility of the MUNU experiment, these results show that it is possible to build much larger TPC's for applications in low energy neutrino physics. In particular, a device with a total $CF_4$ mass of 2 to 8 tons, to be distributed for instance in 4 identical modules, can be contemplated. Such a device, operated at a pressure of 1 to 2 bar, and having a threshold around 100 keV, would be ideally suited to study p–p, $^7$Be and pep neutrinos from the sun. With the given mass range, the event rate would be between 5 to 20 per day. Since not only the electron recoil energy can be measured, but also the scattering angle, the energy of the incident neutrino can be reconstructed. It would thus be possible to perform solar neutrino spectroscopy. That would lead to a major advance in our understanding of solar neutrinos.

## Acknowledgements

to the construction of the pressure equalizing system. This work was supported by INFN, IN2P3 and the Swiss NSF.

## References

[1] B. Kayser et al., Phys. Rev. D 20 (1979) 87.
[2] P. Vogel, J. Engel, Phys. Rev. D 39 (1989) 3378.
[3] M.B. Voloshin, M.I. Vysotskii, L.B. Okun, Sov. Phys. JETP 64 (1986) 446.
[4] M.B. Voloshin, Sov. J. Nucl. Phys. 48 (1988) 804.
[5] K.S. Babu, R.N. Mohapatra, Phys. Rev. Lett. 63 (1989) 228.
[6] M. Leurer et al., Phys. Lett. B 237 (1990) 81.
[7] R. Barbieri et al., Phys. Lett. B 252 (1990) 251.
[8] S.M. Barr, E.M. Friere, A. Zee, Phys. Rev. Lett. 65 (1990) 2626.
[9] B.K. Pal, Phys. Rev. D 44 (1991) 2261.
[10] B.T. Cleveland et al., Nucl. Phys. B (Proc. Suppl.) 38 (1995) 47.
[11] GALLEX collaboration (P. Anselmann et al.), Nucl. Phys. B (Proc. Suppl.) 38 (1995) 68.
[12] J.N. Abdurashitov et al., Nucl. Phys. B (Proc. Suppl.) 38 (1995) 60.
[13] T. Suzuki et al., Nucl. Phys. B (Proc. Suppl.) 38 (1995) 54.
[14] P.I. Krastev, S.T. Petcov, Phys. Lett. B 299 (1993) 94.
[15] E.Kh. Akhmedov et al., A. Lanza, S.T. Petcov, Phys. Lett. B 348 (1995) 124.
[16] J. Pulido, Z. Tao, Phys. Rev. D 51 (1995) 2428.
[17] J.M. Lattimer, J. Cooperstein, Phys. Rev. Lett. 61 (1988) 23.
[18] R. Barbieri, R.N. Mohapatra, Phys. Rev. Lett. 61 (1988) 27.
[19] D. Notzold, Phys. Rev. D 38 (1988) 1658.
[20] J. Bernstein et al., Phys. Rev. 132 (1963) 1227.
[21] P. Sutherland et al., Phys. Rev. D 13 (1976) 2700.
[22] G. Raffelt, Phys. Rev. Lett. 64 (1990) 2856.
[23] V. Castellani, S. Degl'Innocenti, The Astr. Phys. J. 402 (1993) 574.
[24] R.C. Allen et al., Phys. Rev. Lett. 55 (1985) 2401; Phys. Rev. D 47 (1993) 11.
[25] D.A. Krakauer et al., Phys. Lett. B 252 (1990) 177.
[26] B. Achkar et al., Phys. Lett. B 374 (1996) 243.
[27] G. Zacek et al., Phys. Rev. D 34 (1986) 2621.
[28] F. Reines, H.S. Gurr, H.W. Sobel, Phys. Rev. Lett. 37 (1976) 315.
[29] I.I. Gurevitch et al., preprint, I.V. Kurtchatov Institute of Atomic Energy, 123182. Moscow, Russia, 1991; G.S. Vidyakin et al., JETP Lett. 49 (1989) 740.
[30] A.I. Derbin et al., JETP Lett. 57 (1993) 768.
[31] J. Segura et al., Phys. Rev. D 49 (1994) 1633.
[32] B. Achkar et al., Nucl. Phys. B 434 (1995) 503.
[33] H. Wong et al., Phys. Rev. Lett. 67 (1991) 1218.
[34] J.-C. Vuilleumier et al., Phys. Rev. D 48 (1993) 1009.
[35] A. Peisert, F. Sauli, CERN Yellow Report 84-08, 1984; L.G. Christophorou et al., Nucl. Instr. and Meth. 163 (1979) 141.
[36] B. Schmidt, S. Polenz, Nucl. Instr. and Meth. A 273 (1988) 488; K. Martens, Diplomarbeit, Universität Heidelberg, 1989.
[37] C. Broggini et al., Nucl. Instr. and Meth. A 311 (1992) 319.
[38] MUNU collaboration, The MUNU time projection chamber, Nucl. Instr. and Meth. A, submitted.
[39] V. Joergens, Ph.D. thesis, Institut de physique de l'université de Neuchâtel, 1994.
[40] J. Farine, Ph.D. thesis, Institut de physique de l'université de Neuchâtel, 1996.
[41] C. Broggini, Nucl. Instr. and Meth. A 432 (1993) 413.
[42] P. Giarritta, Diplomarbeit, University of Zurich, 1994.
[43] R. Brun et al., GEANT–CERN Program Library.
[44] G. Bagieu, GAMTRACK, ISN–Grenoble Int. Rep. 1992.
[45] N.C. Mukhopadhyay, Phys. Rep. C 30 (1977) 1.
[46] E. Orvini, University of Pavia, private communication.
[47] C. Arpesella, Nucl. Phys. B (proc. suppl) 28A (1992) 420.
[48] Ph. Hubert, University of Bordeaux, private communication.
[49] D. Geiregat et al., Phys. Lett. B 259 (1991) 499.
[50] R. Veenhof, GARFIELD, CERN program library.